Estimating Sub-pixel Surface Roughness Using Remotely Sensed Stereoscopic Data

A. Mushkin*, A. R. Gillespie

ABSTRACT

Surface roughness at the scale of 10^{-2}-10^{1} m can be estimated using the ratio (RR) between surface-reflected solar radiance measured from two view angles at nearly the same time. As RR is primarily a function of the difference between effective sub-pixel shading observed from the two view-angles, the divergence from unity RR values, which are expected for smooth Lambertian surfaces (they have no shadows), was found to be proportional to roughness at the 10^{-2}-10^{1}-m scale of geomorphic desert surfaces. Ground-based RR values at ~1-m resolution, as well as remotely acquired RR values at 4-, 15- and 50-m resolutions, were compared with observed surface roughness in two hyper-arid test sites, located in Death Valley, California USA and the southern Negev Desert in Israel. The ASTER (Advanced Spaceborne Thermal Emission and Reflection Radiometer) 15-m stereoscopic capability is identified as an effective resource for obtaining relative sub-pixel surface-roughness estimates that are largely independent of surface composition and relatively insensitive to atmospheric effects.

# 1.	Introduction

Surface roughness is defined here as the topographic expression of a surface at length scales below the resolution of available digital elevation models or maps. As such, it is commonly identified as a key parameter in many geological, hydrological and planetary studies, as well as an essential variable in remote-sensing applications and climate-prediction models. Because direct measurements of surface roughness are time-consuming and thus unrealistic in large-scale investigations, its characterization from remotely sensed data has been the focus of many previous studies. In this regard, radar backscatter, (e.g., Zebker & Goldstein, 1986; Evans et al., 1992; Weeks et al., 1997) multi-channel VNIR (0.4-1.1 μm) reflectance data (e.g., Li et al., 1998), a combination of both radar and VNIR reflectance (e.g., Evans & Smith 1991; Weeks et al., 1996) and the bidirectional reflectance distribution function (e.g., Hapke, 1984), have all been used to estimate surface roughness. However, a common difficulty in all of these approaches has been that the complexity of natural surfaces commonly exceeds the dimensionality of the data, thus rendering roughness estimates non-unique.

In this study, remotely sensed stereoscopic optical data are used to obtain relative surface-roughness estimates that are largely independent of surface composition and relatively insensitive to atmospheric effects. Developed in a geomorphic context of measuring the textural evolution of low-relief desert surfaces, this approach was tested in the arid environments of Death Valley California, USA and the southern Negev desert of Israel using ground-based measurements at the 1-m scale, MASTER (MODIS-ASTER airborne simulator) stereoscopic data with 4- and 50-m resolution, and ASTER (Advanced Spaceborne Thermal Emission and Reflection Radiometer) 15-m stereoscopic

data. Our results suggest that the ASTER stereoscopic imaging capability is well-suited for obtaining relative measurements of geomorphic roughness variations in such desert environments.

2. Approach

2.1. The Scale of Surface Roughness

As roughness is a scale-dependent property and natural surfaces are inherently complex, universal characterization of surface roughness at all scales requires a large set of parameters such as RMS height, average slope and correlation length (e.g., Shepard et al., 2001; Weeks et al., 1996). However, as different physical processes control the evolution of surface roughness at different scales, the fundamental motivation for a given investigation can determine the relevant scale of surface-roughness and may thus be used to simplify the problem. Because the context of this study is the geomorphic evolution of low-relief desert surfaces, we examine surface-roughness variations at the scale that dominates the textural evolution of such surfaces, i.e., 10^{-2}-10^{1} m (e.g., Amit & Gerson, 1986; McFadden et al., 1989).

Although the spatial resolution of some advanced airborne and spaceborne sensors may be adequate for discriminating surface features below the 1-m scale, surface variations at such scales remain below the resolution limits of most sensors. Consequently, sub-pixel data analyses are commonly required for characterization of surface roughness. In this regard, the unresolved effects of surface-composition have been a major obstacle in the way of robust and stable retrievals of surface roughness estimates from remotely sensed data.

3

2.2. The Stereoscopic Imaging Approach

In this study, we utilize the difference between surface-reflected solar irradiance values measured at two viewing angles and under the same illumination as proxy for relative surface roughness. Assuming that surface elements can be approximated as Lambertian reflectors, surface-leaving VNIR radiance (*L*) at a given view angle (α) can be described as:

$$L_\alpha = \frac{1}{\pi}(I_{sol} + S_\downarrow)R_e(1 - f_{sh(\alpha)}) \tag{1}$$

where L_α is in units of *Wm^{-2}sr^{-1}*. I_{sol} and $S_\downarrow$ are incident solar irradiance and down-welling atmospheric irradiance at the surface, respectively, both in units of *Wm^{-2}*. R_e is surface reflectivity and $f_{sh(\alpha)}$ is the effective aerial fraction of shade at view angle α. Here, we use the term reflectivity as the intrinsic, characteristic material property that describes the ratio between reflected and incident irradiation from a perfectly smooth sample, and the term reflectance as the ratio between reflected and incident irradiation from a rough surface, which can vary according to $f_{sh(\alpha)}$. Following Adams et al. (1989), shade is defined here as the darkening of the surface due to both the presence of unresolved shadows, and increased incidence angle of the solar irradiance. Shade thus defined varies with view angle, even for a Lambertian surface, because the visibility of shadows depends on view angle. Consequently, $f_{sh(\alpha)}$ is thus inherently dependent on the sun-surface-sensor geometry. For example, at constant illumination conditions, shadows seen at nadir viewing will not be visible at a down-sun viewing angle, thus making the surface appear lighter from this angle (Fig. 1). Such lightening is expected to be

proportional to $f_{sh(\alpha=nadir)}$ and surface roughness, and will not occur for perfectly smooth surfaces ($f_{sh}=0$). Furthermore, the ratio ($RR_{\alpha_2}^{\alpha_1}$) between two surface-reflected radiances measured under the same illumination from two view angles α_1 and α_2 is expected to be independent of R_e:

$$RR_{\alpha_2}^{\alpha_1} = \frac{L_{(\alpha_1)}}{L_{(\alpha_2)}} = \frac{\dfrac{1}{\pi}(I_{sol} + S_\downarrow)R_e(1 - f_{sh(\alpha_1)})}{\dfrac{1}{\pi}(I_{sol} + S_\downarrow)R_e(1 - f_{sh(\alpha_2)})} \tag{2}$$

Assuming that R_e does not change with α (Lambetian reflection), and canceling out variables that are independent of α,(I_{sol}, $S_\downarrow$ and R_e), equation 2 can be re-written as:

$$RR_{\alpha_2}^{\alpha_1} = \frac{(1 - f_{sh(\alpha_1)})}{(1 - f_{sh(\alpha_2)})} \tag{3}$$

where perfectly smooth surfaces are expected to display $RR_{\alpha_2}^{\alpha_1} = 1$ ($f_{sh}=0$ at all angles), and increasingly rough surfaces are expected to display $RR_{\alpha_2}^{\alpha_1}$ values diverging from unity, regardless of surface reflectivity (i.e., surface composition).

The geometric sun-surface-sensor configuration determines the sign for the divergence of $RR_{\alpha_2}^{\alpha_1}$ from unity for increasingly rougher surfaces. For example, in the case depicted in Figure 1 $RR_{\alpha_2=nadir}^{\alpha_1=down-sun}$ is expected to increase with increasing roughness because while the denominator in eq. 3 ($L_{\alpha=nadir}$) decreases with roughness (more shading), the numerator ($L_{\alpha=down-sun}$) remains constant because no shadows are visible at this view-angle.

As with all quantitative applications utilizing remotely sensed data, the stereoscopic approach requires corrections for atmospheric effects. Equation 4 describes the main atmospheric effects present in remote measurements of L_α:

$$L_{(\alpha)}^* = L_{(\alpha)}\tau_{(\alpha)} + S_{(\alpha)}^\uparrow \qquad (4)$$

where L_α^* is the at-sensor radiance in units of $Wm^{-2}sr^{-1}$ measured above the surface at view angle α, and τ and $S^\uparrow$ are atmospheric transmissivity (unitless) and path radiance ($Wm^{-2}sr^{-1}$), respectively. $RR_{\alpha_2}^{\alpha_1}$ as measured from an airborne or spaceborne sensor ($RR*_{\alpha_2}^{\alpha_1}$) should therefore be expressed as:

$$RR*_{\alpha_2}^{\alpha_1} = \frac{L_{(\alpha_1)}^*\tau_{(\alpha_1)} + S_{(\alpha_1)}^\uparrow}{L_{(\alpha_2)}^*\tau_{(\alpha_2)} + S_{(\alpha_2)}^\uparrow} \qquad (5)$$

where τ and $S^\uparrow$ are dependent on α because the atmospheric path-length between the surface and the sensor changes with α. Although the additive terms in equation 5 (i.e., $S^\uparrow$) can be removed with simple techniques such as 'dark-object subtraction', corrections for τ are more complex because they require calibration against known spectra or re-scaling of the data using model-derived approximations of $\tau_{(\alpha)}$, such as calculated with MODTRAN (Ontar, 2001). However, after removal of the additive terms $S_{\alpha_1}^\uparrow$ and $S_{\alpha_2}^\uparrow$, equation 5 is reduced to:

$$RR*_{\alpha_2}^{\alpha_1} = \frac{\tau_{(\alpha_1)}}{\tau_{(\alpha_2)}} RR_{\alpha_2}^{\alpha_1} \qquad (6)$$

where $\tau_{(\alpha_1)}/\tau_{(\alpha_2)}$ is a scaling factor that is uniform across the image and therefore of minor significance to relative roughness estimations within a single image. Consequently, the stereoscopic approach does not require corrections for atmospheric transmissivity.

Roughness variations measured with this approach inherently incorporate all sub-pixel scales because f_{sh} represents shading integrated over all scales within the pixel. Consequently, the spatial resolution of the stereoscopic data determines the upper limit for the scale of roughness variations that can be detected.

3. Methods

3.1. Numerical Simulations

Atmosphere-free simulations of ground-reflected solar irradiance from simplified surfaces at variable roughnesses, reflectivities and illumination angles were used to identify some of the basic characteristics and limitations of the stereoscopic approach. While recognizing that a one-dimensional representation is inadequate for describing the roughness of natural surfaces, we use the RMS height of evenly spaced surface elements as a single-parameter approximation to describe the roughness of the simplified surfaces used in our numerical models.

3.2. Test sites

Two test sites located in arid environments were selected for this study: (1) Trail Canyon fan and the adjacent playa deposits in Death Valley, California USA and (2) the Raham fan and the nearby Yotvata playa in the southern Negev desert of Israel. At both sites, vegetation mainly occurs in the active channels or at well-constrained localities

within the playas. Otherwise it accounts for less than 3% of the surface and mainly consists of desert shrubs (< 1 m) and some Acacia trees on the Raham fan. Alluvial surfaces in both sites display a trend of decreasing roughness with increasing age, and together with playa deposits ranging from salt flats to chaotic salt pillar (~1 m in height) terrain, provide a wide range of surface roughness variations mainly occurring between conveniently large ($>10^2$ m) geomorphic units that display relatively small internal roughness variations. Remotely acquired stereoscopic roughness estimates over these test sites were compared with geomorphic maps of Trail Canyon fan (Gillespie et al., 1984), the Raham fan (Crouvi, 2002) and with ground observations.

3.3. Field Measurements

A portable goniometer (Fig. 2) was designed for stereoscopic imaging of the surface in the field. Two sensors that can be fixed at any given angle between 90° and -30° from nadir along an upright aluminum arch 2 m in diameter, which can pivot 360° around a tripod, enable replication of airborne or spaceborne stereoscopic measurements at the ~1-m scale along a selected azimuth track. Goniometer-derived $RR^{\alpha_1}_{\alpha_2}$ values are readily compared with ground-measured surface profiles, as well as with concurrent satellite-derived $RR^{\alpha_1}_{\alpha_2}$ values. Goniometer measurements in the Death Valley test site were acquired on October 24th, 2003 during the MASTER overflight (see details below).

3.4. Remotely Sensed Data

The stereoscopic approach was applied using data acquired by the MASTER and ASTER sensors, which are briefly described below.

8

ASTER is a multispectral sensor (Yamaguchi et al., 1998) on board the Terra satellite. It acquires 14 channels of data between 0.56 and 11.5 μm and has a ~60-km swath. The spatial resolution (pixel footprint) of the three VNIR channels between 0.56-0.81 μm is 15 m, whereas the six SWIR channels located between 1.65 and 2.4 μm have 30-m spatial resolution, and the five TIR channels between 8.1 and 11.5 μm are acquired at 90-m spatial resolution. The ASTER sensor has a stereoscopic imaging capability made possible by an additional channel (3B) of 15-m data that is acquired at the same wavelengths as the 3rd VNIR nadir channel (3N) at ~0.81 μm, but ~55 seconds later looking back 27.6° from nadir. Although 3B data were primarily designed for independent generation of ~30-m DEM's, which are available as a validated standard ASTER product, unregistered channel 3B data are included with nearly all ASTER level-1B data sets. Thus, combined with the 3N data, the ASTER 3B data comprise an important resource for the testing and general application of the stereoscopic approach to estimating sub-pixel surface roughness. The southward daytime track of the Terra satellite in its near-polar orbit implies that ASTER-derived $RR_{\alpha_2}^{\alpha_1}$ values, where α_1=ASTER 3B and α_2=ASTER 3N, are expected to be positively correlated with surface roughness for the test sites examined in this study, i.e., at mid-latitudes in the northern hemisphere. The correlation between $RR_{\alpha_2}^{\alpha_1}$ values and surface roughness is dependent on the sun-surface-senor phase angle (Fig. 1).

The ASTER data set used over the Death Valley test site was acquired on November 12th 2001, while the sun was 38° above the horizon. The ASTER data set used for the Raham test site was acquired on April 6th 2001 while the sun was 63° above the horizon.

MASTER is an airborne sensor (Hook et al., 2001) designed as a demonstration instrument for the ASTER and MODIS sensors. It acquires 50 channels of data in the VIS-TIR wavelengths (i.e., 0.45-11.9 μm) and a ±22.5° swath. MASTER does not have built-in stereoscopic imaging capability and thus stereoscopic data sets were generated from parallel flight lines acquired ~10 minutes apart and spatially offset from each other to replicate the ASTER stereoscopic view angle. Two such data sets were generated in October 2003 over Trail Canyon fan in the Death Valley test site. The first data set was acquired on October 10, 2003 while sun elevation was ~44° above horizon. The sensor was flown at an altitude of ~1.5 km above terrain, yielding an IFOV of ~4 m. The phase angle between the two side-lapped images was ~20° over the Trail Canyon fan. The second MASTER stereoscopic data set was acquired on October 25, 2003 with the sun ~35° above the horizon. In this case the sensor was flown on an ER2 at an altitude of ~20 km above terrain, yielding a pixel footprint of ~50 m. The stereoscopic phase angle was ~30° between the two images over the test site.

For both the ASTER and MASTER sensors the time delay between stereoscopic data acquisition of ~55 seconds and ~10 minutes, respectively, is ignored and solar illumination is regarded as constant.

4. Results

4.1. Numerical Simulations

In Figure 3, contours of ground-reflected solar irradiance values are plotted as a function of sensor-angle from nadir on the x axis and roughness (RMS) on the y axis. The

radiance contours form a diagonally sloping concave surface converging to minimal values at the top left corner, which represents the highest RMS values and the most oblique view angles looking 'up-sun'.

Radiance values at 30° down-sun viewing are plotted vs. radiance values at nadir viewing in Figure 4. In this field, $RR_{\alpha_2}^{\alpha_1}$ is the slope of the straight lines representing surfaces with a common RMS but variable reflectivities. These 'iso-roughness' lines converge towards the origin because the contrast between sunlit and shadowed surface elements is inversely proportional to reflectivity, where the radiance measured above completely non-reflective surfaces is expected to be zero at both view-angles. The two selected solar illumination scenarios illustrate that $RR_{\alpha_2=nadir}^{\alpha_1=30^0}$ values for high solar elevations are expected to be different and more tightly clustered than $RR_{\alpha_2=nadir}^{\alpha_1=30^0}$ values for low solar elevations (discussed below).

4.2. Ground Measurements

Goniometer-based $RR_{\alpha_2=nadir}^{\alpha_1=30^0}$ values at the ~1-m scale and at a 20° NE azimuthal path (similar to the path of the Terra satellite) are plotted against representative RMS values for the same surfaces in Figure 5. As expected, $RR_{\alpha_2=nadir}^{\alpha_1=30^0}$ values close to unity for nearly flat surfaces generally increase together with surface RMS, thus displaying a positive correlation between the two parameters.

4.3. Death Valley Test Site

Figure 6 displays a co-registered set of: 1) the Trail Canyon fan geomorphic map, 2) an ASTER panchromatic image and 3) a grayscale roughness image derived from ASTER 15-m stereoscopic data (Figs. 6a,b & c, respectively). In this roughness image white corresponds to high $RR^{*\alpha_1}_{\alpha_2}$ values (i.e., relatively rough surfaces) and black to unity $RR^{*\alpha_1}_{\alpha_2}$ values (i.e., smooth surfaces). ASTER-derived 15-m $RR^{*\alpha_1}_{\alpha_2}$ values (i.e., $^{15m}RR^{*\alpha_1}_{\alpha_2}$) correlate well with geomorphic units Q_2 and Q_3 (i.e., low $^{15m}RR^{*\alpha_1}_{\alpha_2}$ values for the smooth Q_2 surfaces and higher $^{15m}RR^{*\alpha_1}_{\alpha_2}$ values for the rougher Q_3 surfaces), and also reveal the roughness variations between the smooth salt-flats and the chaotic salt-pillar terrain in the playa deposits east of the fan terraces (Fig. 6c). In contrast, the active stream-channels do not display characteristic $^{15m}RR^{*\alpha_1}_{\alpha_2}$ values, but rather high-frequency variations between smooth and rough surfaces. Higher-resolution, 4-m MASTER data (Fig. 7a) are sufficient to resolve these variations as alternations between smooth sand-bars and rougher surfaces, which display similar MASTER-derived 4-m $RR^{*\alpha_1}_{\alpha_2}$ values (i.e., $^{4m}RR^{*\alpha_1}_{\alpha_2}$) to the Q_3 surfaces (Fig. 7b). $^{4m}RR^{*\alpha_1}_{\alpha_2}$ values also enable detection of more subtle roughness variations such as those between the dirt road and the alluvial terraces, which it crosses (Fig. 7). MASTER-derived 50-m $RR^{*\alpha_1}_{\alpha_2}$ values (i.e., $^{50m}RR^{*\alpha_1}_{\alpha_2}$, not shown here) display a poor correlation with geomorphic units Q_2 and Q_3, yet they do reflect the roughness variations between the smooth salt-flats and the chaotic salt-pillar surfaces.

4.4. Raham Fan Test Site

Figure 8 displays a co-registered set of: 1) the Raham fan geomorphic map, 2) an ASTER panchromatic image and 3) a grayscale roughness image derived from ASTER 15-m stereoscopic data (Figs. 8a,b & c, respectively). The ASTER derived $RR^{*\alpha_1}_{\alpha_2}$ values at 15-m spatial resolution are in good agreement with the age-dependant roughness of the geomorphic map units of the Raham alluvial fan. The older and smoother geomorphic units display relatively low $^{15m}RR^{*\alpha_1}_{\alpha_2}$ values, as do the asphalt roads in the center of the image, whereas the younger, rougher units display relatively high $^{15m}RR^{*\alpha_1}_{\alpha_2}$ values.

5.   Discussion

5.1. Fundamental Limitations

Stereoscopic data sets allow us to calculate $RR^{\alpha_1}_{\alpha_2}$ values for each pixel in an image. Yet, these values should not be automatically regarded as physically meaningful estimates of surface roughness, because they do not represent a direct measure of this surface property, but rather a measure of the difference between f_{sh} at the two view angles (Eq. 3). Using variations in $RR^{\alpha_1}_{\alpha_2}$ values as a proxy for actual roughness variations on the surface is therefore limited to cases in which variables other than surface roughness affecting f_{sh} (i.e., illumination angle, and view angle) remain constant. This restriction is demonstrated in Figure 3 in which the concave diagonally dipping surface defined by the contours of ground-reflected radiance implies that α_1 and α_2 as well as $\Delta\alpha$, affect $RR^{\alpha_1}_{\alpha_2}$ values. For example, at a given RMS (y axis values are constant), $RR^{\alpha_1=30^O}_{\alpha_2=nadir}$

is different from $RR_{\alpha_2=-30^o}^{\alpha_1=nadir}$. The practical implication of this is that $RR_{\alpha_2}^{\alpha_1}$ values reflect

relative surface-roughness variations only between surfaces with similar slopes within the

scene. We therefore limit our application of this approach, at this stage, to flat-lying

surfaces, and use empirical calibrations to relate the $RR_{\alpha_2}^{\alpha_1}$ values to actual surface

roughness.

Random measurement error ("noise") imposes an additional constraint on practical

application of the stereoscopic approach. Although $RR_{\alpha_2}^{\alpha_1}$ values are theoretically

independent of surface composition (Eq. 3), Figure 4 illustrates that roughness variations

between two surfaces can be detected only as long as the distance between their lines in

the L_{α_1} vs. L_{α_2} field is greater than actual measurement noise. Consequently, roughness

estimates over low-reflectivity surfaces may become dominated by noise due to the

convergence of the 'iso-roughness' lines, which occurs over such surfaces. However, this

complication can be ameliorated by utilizing data acquired at low sun-elevations: the

larger shadows cast under such conditions result in a larger difference between L_{α_1} and

L_{α_2}. Thus, while $RR_{\alpha_2}^{\alpha_1}$ values for perfectly smooth surfaces remain at unity, separation

between $RR_{\alpha_2}^{\alpha_1}$ values for rough surfaces increases and sensitivity to measurement noise at

low reflectivities decreases (Fig 4). An $RR_{\alpha_2}^{\alpha_1}$ image of Trail Canyon fan derived from an

ASTER image acquired on June 1, 2001 at sun elevation of ~75° (not shown here) proved

to be noise-dominated, revealing no roughness variations within the scene. In contrast,

the ASTER-derived $RR_{\alpha_2}^{\alpha_1}$ image of the same area acquired November 12th 2001 (sun

elevation of 36°) revealed the surface-roughness variations presented in Figure 6c.

14

Numerical simulations (not shown here) suggest that data acquisition along the principle solar illumination plane at the time of acquisition maximizes the difference between L_{α_1} and L_{α_2}, and may therefore offer an additional option to reduce the effects of measurement noise and improve the detectability of surface roughness variations using the stereoscopic approach.

The approach presented in this paper is part of a suite of feasible, yet relatively un-exploited methods of estimating surface roughness using repetitive data over the same surface. Although we realize the potential in estimating surface roughness from temporal variations of sub-pixel shade, such as captured in morning/afternoon or winter/summer image pairs, we prefer to use the multi-angle variations as discussed in this paper. The wide availability of data, significantly decreased risk of unresolved compositional changes on the surface, and the relative insensitivity to atmospheric effects outweigh, in our view, the limitations that may arise from high-sun elevations at the time of stereoscopic data acquisition.

5.2. Roughness Estimates at Different Scales

Previous studies have shown that a one-dimensional universal characterization of the roughness of natural surfaces is inadequate and that as many as five independent parameters may be required for such a task (e.g., Weeks et al., 1996). In the geomorphic context and the roughness scales of the field measurements conducted in this study (i.e., ~1 m) RMS height appears to be a satisfactory, 1st-order description of the roughness of the Trail Canyon alluvial fan surfaces. However, although a good correlation was established between ground-measured $RR_{\alpha_2}^{\alpha_1}$ values and representative RMS height at the

1-m spatial scale (Fig. 5), the complexity of obtaining such representative RMS values for larger-scale surface areas (e.g., 4-15 m) prevents the extension of similar correlations to remotely sensed $RR_{\alpha_2}^{\alpha_1}$ values, at this stage of our study. Instead, we compare the latter with the age-dependent roughness of alluvial fan surfaces in the study areas and with observed roughness variations in the playa deposits. Excluding the active channel of Trail Canyon fan, ASTER-derived 15-m $RR_{\alpha_2}^{\alpha_1}$ values ($^{15m}RR^{*\alpha_1}_{\alpha_2}$) show a good correlation with fan-surface age and thus with surface roughness in both test sites (Figs. 6, 7 & 8). Similar $^{15m}RR^{*\alpha_1}_{\alpha_2}$ values that are close to unity between heavily varnished, smooth Q_2 alluvial surfaces on Trail Canyon fan and highly reflective salt flats in the nearby playa (Fig. 6), suggest that remotely acquired $RR_{\alpha_2}^{\alpha_1}$ values are in practice independent of surface reflectivity. Detection of roughness variations between Q_2 and Q_3, in places where they display a similar brightness in the panchromatic image (Fig. 6), further demonstrate the added value roughness estimates using this approach.

Comparison between the 50-, 15- and 4-m $RR_{\alpha_2}^{\alpha_1}$ images and the geomorphic map of the Trail Canyon fan reveals that the 50-m roughness estimates (not shown here) do not correlate with the age-dependent surface roughness as mapped by Gillespie et al. (1984) nor are they consistent with the 4- and 15-m data. It appears that $^{50m}RR^{*\alpha_1}_{\alpha_2}$ values over the Trail Canyon fan incorporate surface roughness variations that are not age-dependent, and that such data are not adequate for geomorphic roughness mapping in such environments. In contrast, $^{4m}RR^{*\alpha_1}_{\alpha_2}$ values display a good correlation with the geomorphic map units, as well as with finer-scale roughness variations, e.g., the gravel

16

road (~4-m wide) in the lower part of Figure 7, which shows up as brighter (rougher) than the background on the relatively smooth Q_2 surfaces and darker (smoother) than its background on the rougher Q_3 surfaces. Whereas the 4-m roughness estimates offer finer details, they are generally consistent with the 15-m roughness estimates, thus suggesting that the latter are sufficient for geomorphic roughness mapping. Nonetheless, this is not the case for the active channel, where the presence of vegetation (~20% cover) and high frequency (<10 m) variations between sand bars, gravel bars and swales yield inconsistent 15-m roughness estimations. Here, the finer resolution of the 4-m data is required to map the smooth sand bars with no vegetation (light patches in Fig. 7a), which appear in Figure 7b as dark areas with lower $^{4m}RR^{*\alpha_1}_{\alpha_2}$ values. The effect of vegetation on

$^{4m}RR^{*\alpha_1}_{\alpha_2}$ in the gravel bars and swales remains unconstrained. Furthermore, the effect of vegetation in general on the stereoscopic roughness estimates requires further research, although preliminary analyses suggest that the ASTER stereoscopic data at ~0.81 μm are especially sensitive to vegetation cover and that data at other wavelengths may be less affected.

6. Summary and conclusions

We suggest the stereoscopic approach as a simple and effective method estimate relative roughness variations over of low-relief bare surfaces. Stereoscopic roughness estimates at the 4- and 15-m scale were found to be in agreement with age-dependent geomorphic roughness and with roughness observed in the field. In this respect, the ASTER 15-m stereoscopic capability is identified as an effective and readily accessible resource for such surface-roughness estimations. Our results support the findings of

17

Weeks et al. (1996) that surface reflectance is dominated by surface roughness at the 10^{-2}-10^1 m scale. However, we do not attempt at this stage to invert our measurements with universal surface roughness models. Roughness variations measured with the stereoscopic approach are relative in nature, require local calibration and are thus consistent only within a single image. Yet, as they are largely independent of surface composition and fairly insensitive to atmospheric effects, stereoscopic roughness estimates provide a simple and robust tool that can benefit a wide range of Earth science disciplines.

References

Adams, J. B., Smith, M. O., and Gillespie, A. R. (1989). Simple models for complex natural surfaces: A strategy for the hyperspectral era of remote sensing. *Proc. IEEE International Geosciences Remote Sensing Symposium* I, 16-21.

Amit, R., and Gerson, R. (1986). The evolution of Holocene reg (gravelly) soil in deserts - an example from the Dead Sea region. *Catena* 13, 59-79.

Crouvi, O. (2002). "Geomorphic Mapping Using Hyperspectral Remote Sensing: The Wadi Raham Alluvial Fan as a Case Study." MsC thesis, Hebrew University, Jerusalem.

Evans, D. L., Farr, T. G., and van Zyl, J. J. (1992). Estimates of surface roughness derived from synthetic aperture radar (SAR) data. *IEEE Transactions on Geoscience and Remote sensing* 30(2), 382-389.

Evans, D. L., and Smith, M. O. (1991). Separation of vegetation and rock signatures in thematic mapper and polarimetric SAR images. *Remote Sensing of Environment* 37, 63-75.

Gillespie, A. R., Kahle, A. B., and Palluconi, F. D. (1984). Mapping alluvial fans in Death Valley, California, using multispectral thermal infrared images. *Geophysical Research Letters* 11, 1153-11556.

Hapke, B. (1984). Biderectional reflectance spectroscopy. *Icarus* 59, 41-59.

Hook, S., Myers, K., Thome, M., Fitzgerald, M., and Kahle, A. B. (2001). The MODIS/ASTER Airborne Simulator (MASTER)—a new instrument for earth science studies. *Remote Sensing of Environment* 76, 93-102.

Li, W.-H., Weeks, R. J., and Gillespie, A. R. (1998). Multiple scattering in the remote sensing of natural surfaces. *International Journal of remote Sensing* 19(9(1725-1740.

McFadden, L. D., Ritter, J. B., and Wells, S. G. (1989). Use of Multiparameter Relative-Age Methods for Age Estimations and Correlation of Alluvial Fan Surfaces on a Desert Piedmont, Eastern Mojave Desert, California. *Quaternary Research* 32, 276-290.

Ontar. (2001). PcModWin v 4.0, North Andover, MA 01845, USA.

Shepard, M. K., Campbell, B. A., Bulmer, M. H., Farr, T. G., Gaddis, L. R., and Plaut, J. J. (2001). The roughness of natural terrain: a planetary and remote sensing perspective. *Journal of Geophysical Research* 106(E12), 32,777-32,795.

Weeks, R. J., Smith, M. O., Pak, K., and Gillespie, A. R. (1997). Inversions of SIR-C and AIRSAR data for the roughness of geological surfaces. *Remote Sensing of Environment* 59, 383-396.

Weeks, R. J., Smith, M. O., Pak, K., Li, W.-H., Gillespie, A. R., and Gustafson, W. (1996). Surface roughness, radar backscatter, and visible and near-infrared reflectance in Death Valley, California. *Journal of Geophysical Research* 101(E10), 23,077-23,090.

Yamaguchi, Y., Kahle, A. B., Tsu, H., Kawakami, H., and Pniel, M. (1998). Overview of Advanced Spaceborne Thermal Emission and Reflection radiometer (ASTER). *IEEE Transactions on Geoscience and Remote Sensing* 36(4), 1062-1071.

Zebker, H. A., and Goldstein, R. M. (1986). Topographic mapping from interferometric synthetic aperture radar observations. *Journal of Geophysical Research* 91(B5), 4993-4999.

Figure Captions:

Fig. 1. Schematic illustration of the stereoscopic approach for estimating sub-pixel surface roughness. Under constant illumination conditions pixel DN values are controlled by sub-pixel shading. A pixel in the rough section of the surface viewed up-sun (view angle *a*) will have a lower DN value than the same pixel viewed from nadir (view angle *b*), because more shadows are visible from the up-sun view angle. Similarly, the same pixel viewed down-sun (view angle *c*) will have higher DN values than from nadir viewing. DN values for pixels in the smooth section of the surface will not change with view angle because there is no shading. Accordingly, the difference between DN values of corresponding pixels, instantaneously recorded from different view angles can be used as a proxy for sub-pixel surface roughness.

Fig. 2. A portable goniometer enables stereoscopic data acquisition in the field at the ~1-m scale.

Fig. 3. Numerical simulations for ground-reflected solar radiance as a function of viewing angle and surface roughness (RMS height of the surface elements). Sun elevation, incident solar irradiation and surface reflectivity for all simulations were fixed at 60°, 100 Wm^{-2} and 90%, respectively. Contours represent radiance values in units of $Wm^{-2}sr^{-1}$.

Fig. 4. Measured radiance at nadir vs. measured radiance at 30° down sun. (A) Sun elevation = 60°, (B) sun elevation = 35°. The straight lines represent surfaces of the same roughness and the symbols represent surface reflectivity. The slope of these 'iso-roughness' lines is the ratio (*RR*) between the radiance values as measured at the two view-angles and can be used as an estimate for surface roughness. Although *RR* is theoretically independent of surface reflectivity the shaded circles, which represent theoretical measurement noise, illustrate that lower sun elevations (i.e., larger shadows) can improve the detectability of roughness variations using the stereoscopic approach (see text for details).

Fig. 5. Measured RMS of surface elements vs. the ratio between radiance values measured with the goiniometer (Fig. 2) at 30° and nadir viewing. Dashed lines represent the estimated errors for measurements.

Fig. 6. Co-registered geomorphic map of Trail Canyon fan (modified from Gillespie et al., 1984) (a), ASTER panchromatic (0.56-0.81 μm) image (b), and stereoscopic roughness estimates derived from ASTER 15-m data acquired on November 12th 2001 (c). Dashed line in *b* marks the location of Fig. 7. Dark colors in *c* represent a low 3B/3N ratio (i.e., smooth surfaces) and bright colors represent higher ratios (i.e., rough surfaces). Location 1 - Q_2 is only subtly darker than Q_3 in the panchromatic image, whereas the roughness image clearly distinguishes between the two. Location 2 - the Q_2 surfaces appear brighter than the Q_3 surfaces east of them in the panchromatic image, whereas the roughness image facilitates a correct identification of these units.

Fig. 7. Co-registered high-resolution (4 m) panchromatic MASTER image of the Trail Canyon fan active stream-channel and adjacent terraces (a), and stereoscopic roughness estimates derived from the MASTER 4-m data (b). The MASTER stereoscopic ratio image was generated from two side-lapped images (see text for details). Dark colors represent a low 3B/3N ratio (i.e., smooth surfaces) and bright colors represent higher ratios (i.e., rough surfaces).

Fig. 8. Co-registered geomorphic map of Raham fan (modified from Crouvi 2002) (a), ASTER panchromatic (0.56-0.81 µm) image (b), and stereoscopic roughness estimates derived from ASTER 15-m data acquired on April 6th 2001 (c). Dark colors represent a low 3B/3N ratio (i.e., smooth surfaces) and bright colors represent higher ratios (i.e., rough surfaces).

Figure 1
Click here to download high resolution image
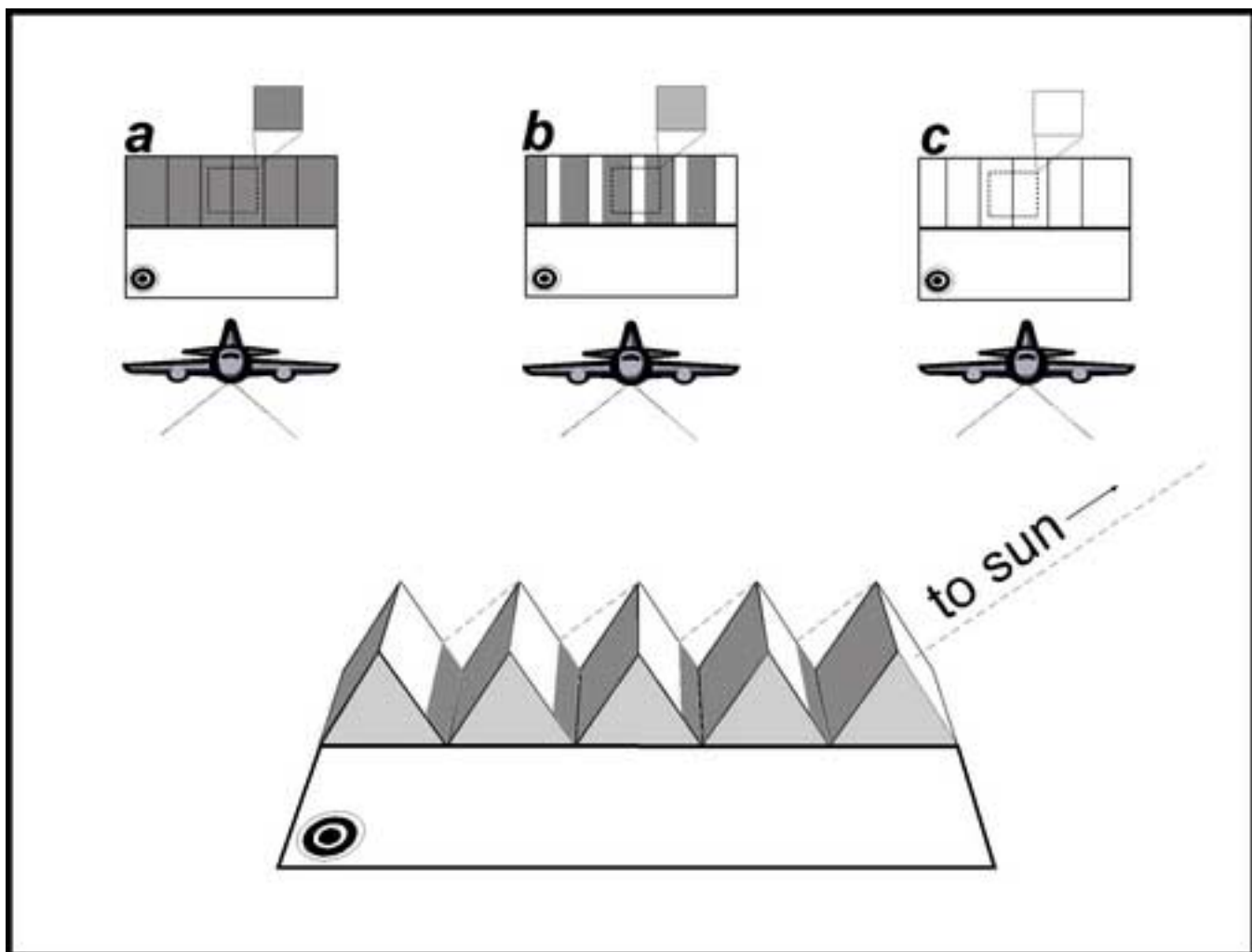
Figure 2
Click here to download high resolution image
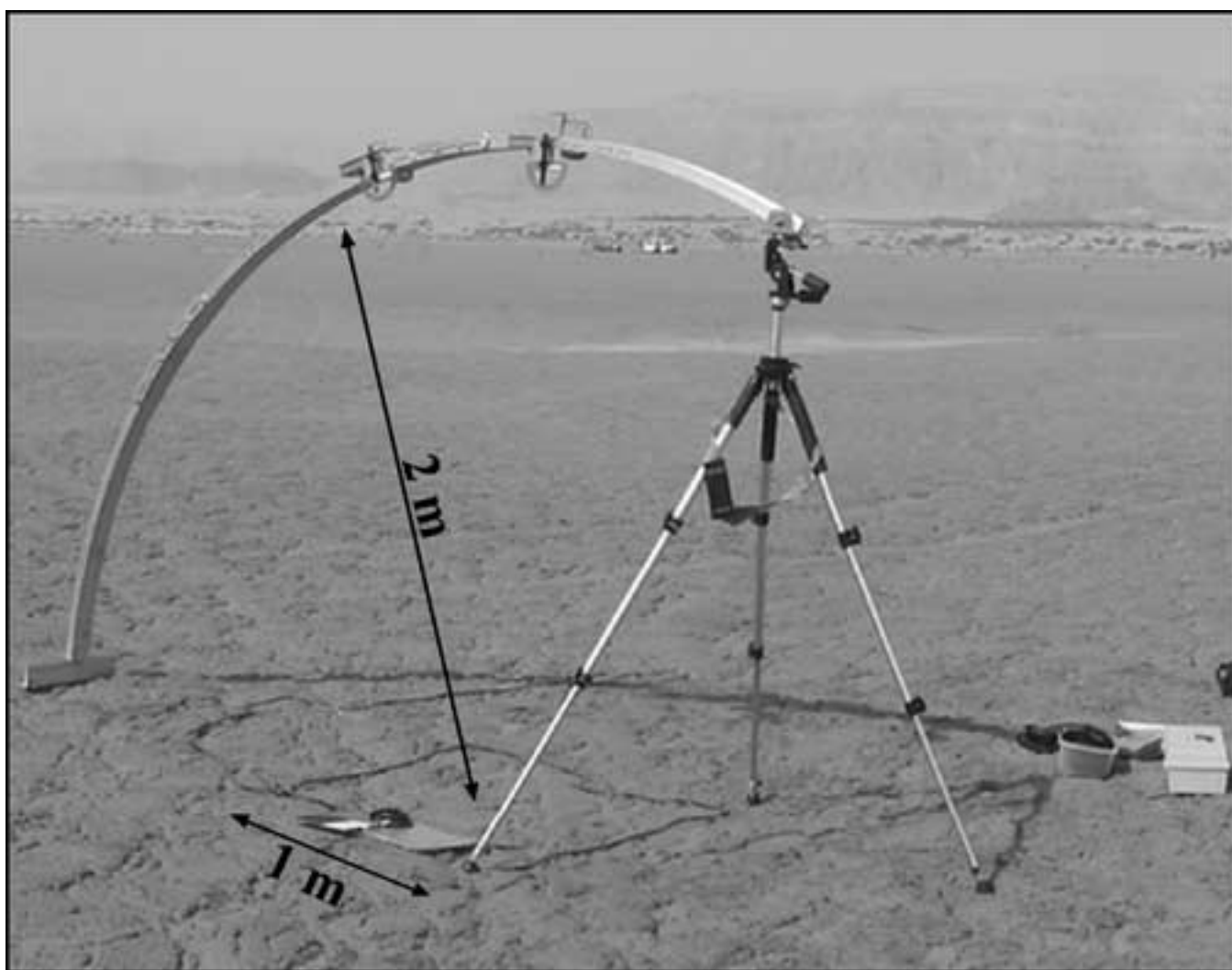
Figure 4
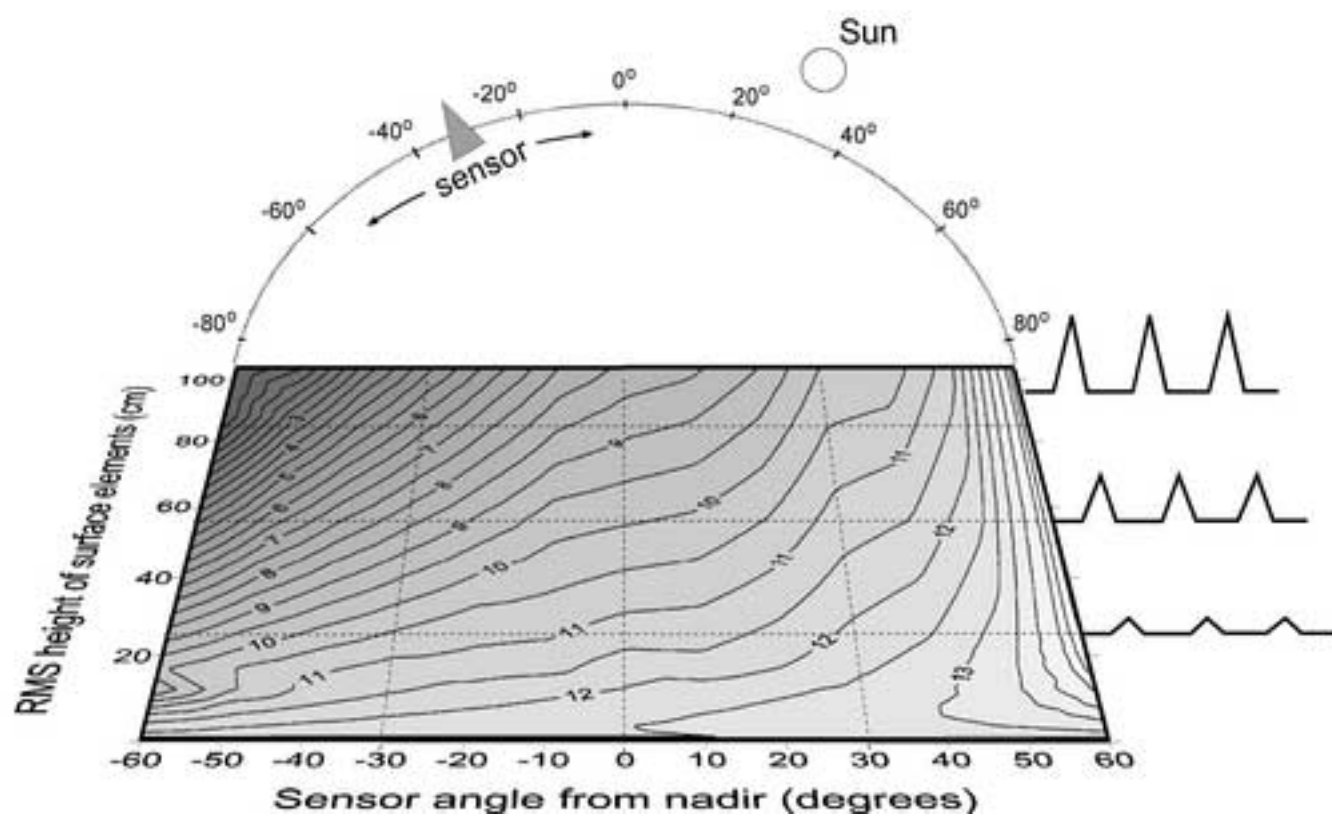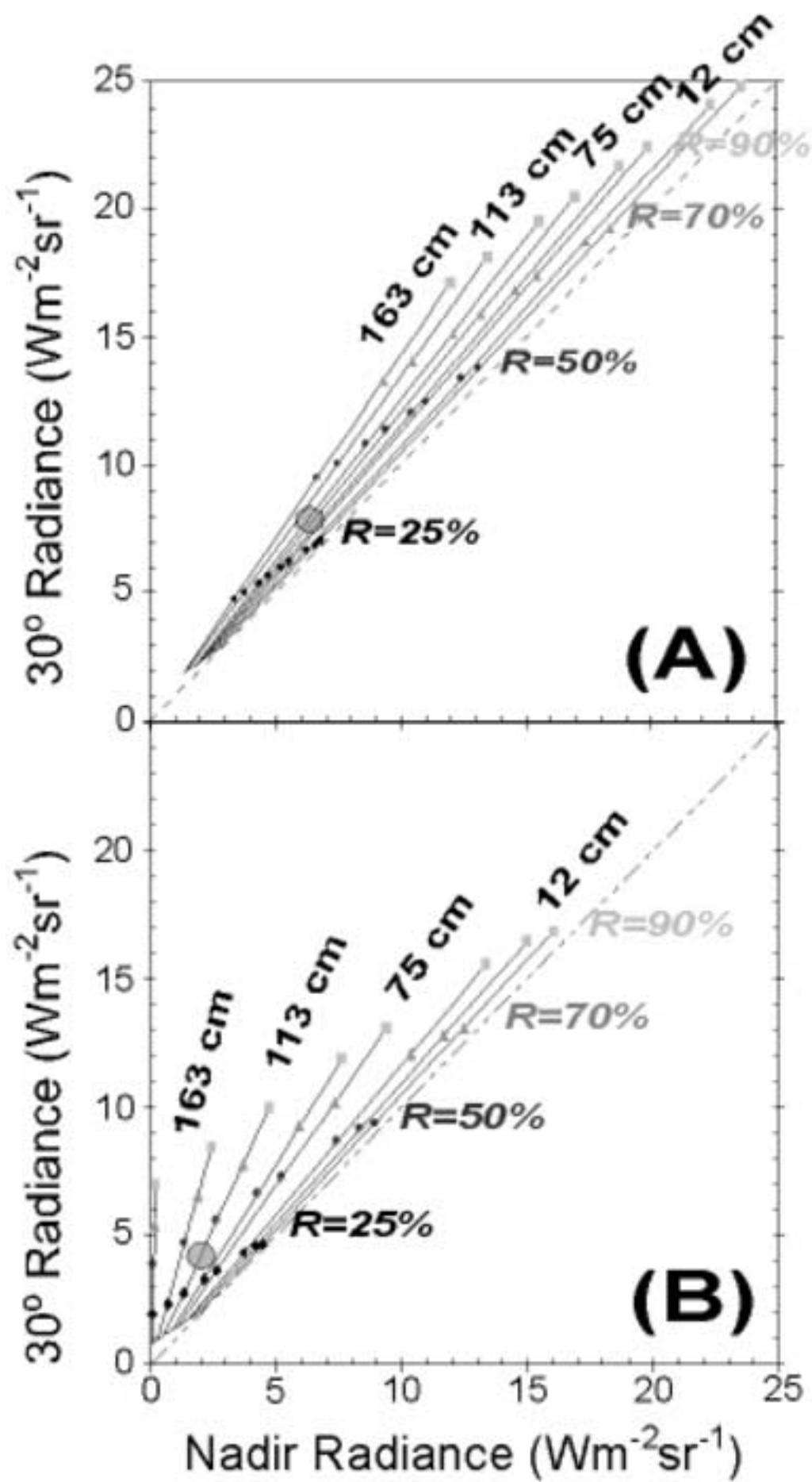**Click here to download high resolution image**

Figure 5
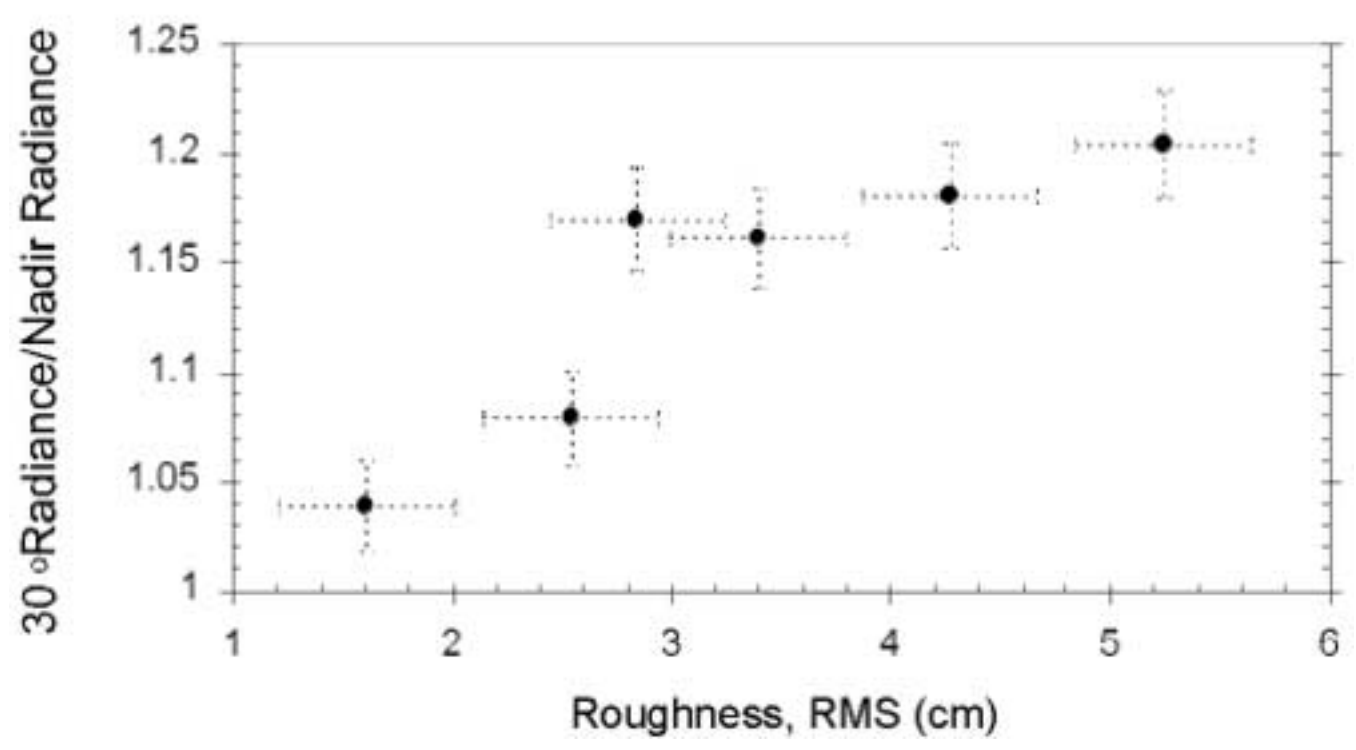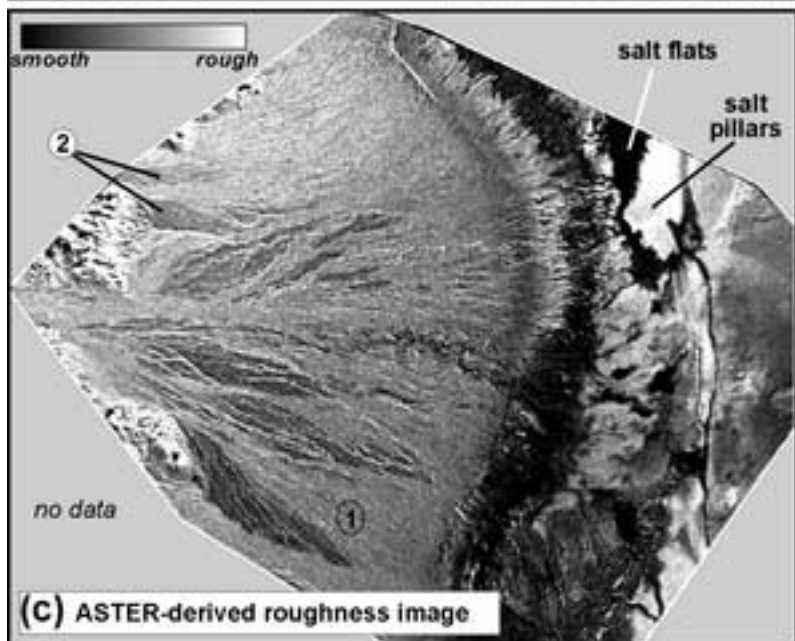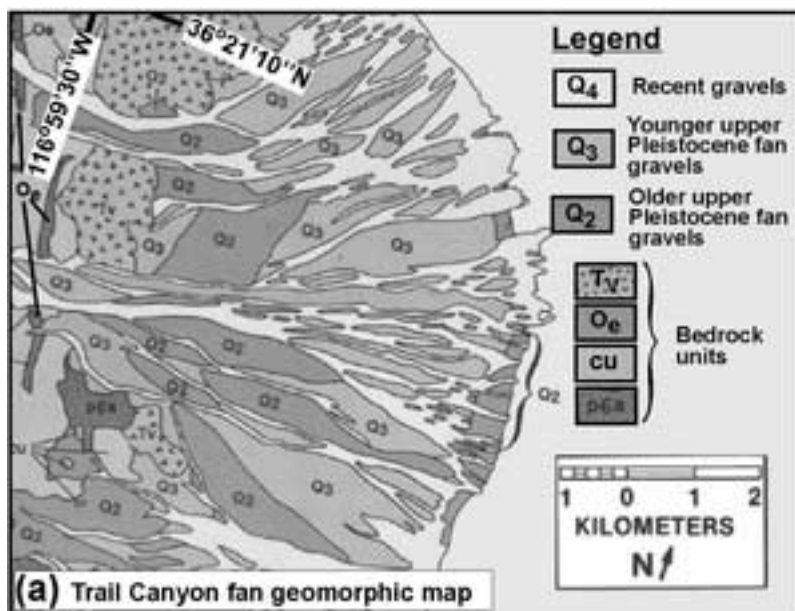**Click here to download high resolution image**

Figure 5

Figure 6
[Click here to download high resolution image](#)

(a) Trail Canyon fan geomorphic map

Legend

Q4	Recent gravels
Q3	Younger upper Pleistocene fan gravels
Q2	Older upper Pleistocene fan gravels
Tv	Bedrock units
Oe	
cu	
p-Ca	

1 0 1 2
KILOMETERS
N

(b) ASTER panchromatic image

salt flats
salt pillars

(c) ASTER-derived roughness image

smooth   rough
no data
salt flats
salt pillars
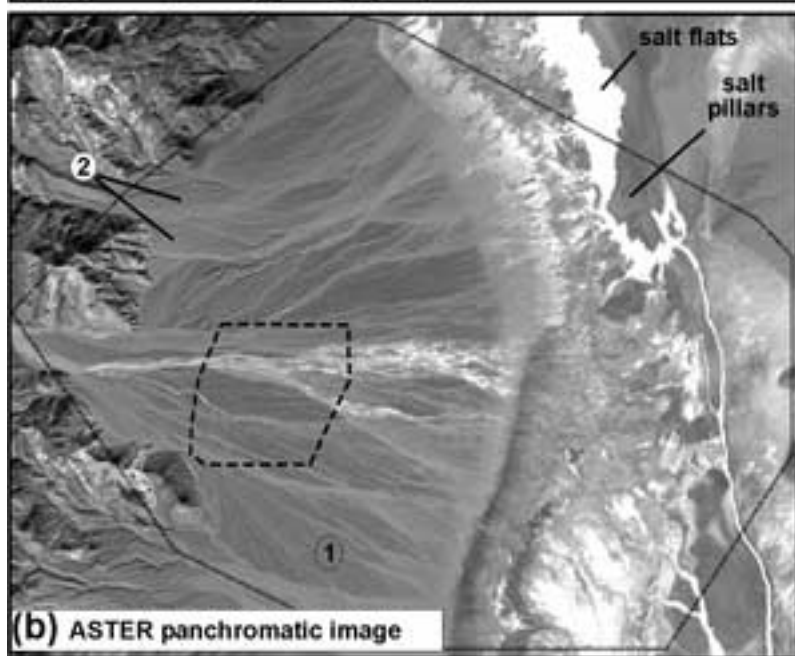
Figure 7
[Click here to download high resolution image](#)

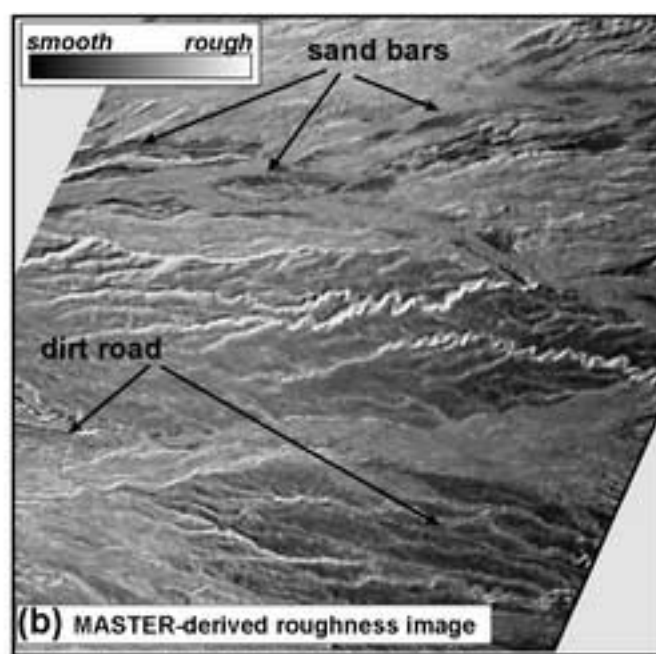(a) MASTER panchromatic image
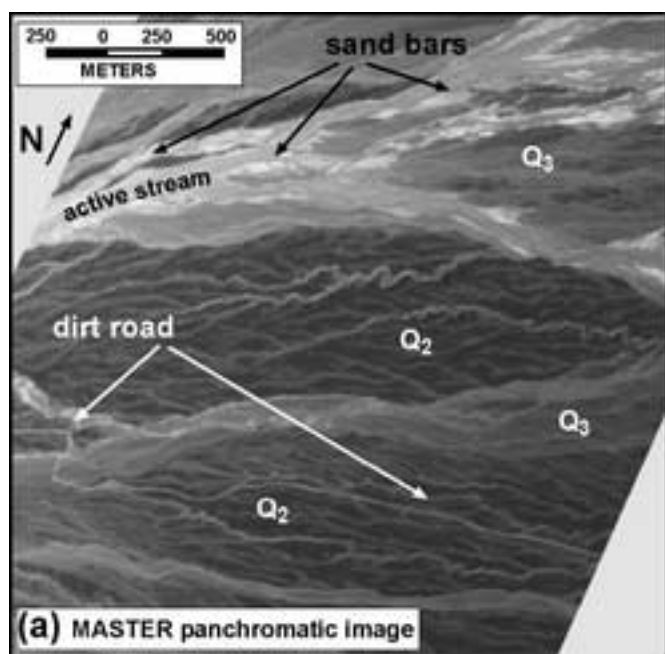
(b) MASTER-derived roughness image

Figure 8
[Click here to download high resolution image](#)

(a) Raham fan geomorphic map
(b) ASTER panchromatic image
(c) ASTER-derived roughness image